AGU PUBLICATIONS

JGR

Journal of Geophysical Research: Earth Surface

RESEARCH ARTICLE

10.1002/2014JF003189

This article is a companion to *Buscombe et al.* [2014] doi:10.1002/2014JF003191.

Key Points:
- Methods are presented to statistically analyze riverbed acoustic backscatter
- Creation of high-resolution maps of spectral properties from corrected echoes
- Clear relationship between spectral properties and smooth/rough areas of the bed

Correspondence to:
D. Buscombe,
dbuscombe@usgs.gov

Citation:
Buscombe, D., P. E. Grams, and M. A. Kaplinski (2014), Characterizing riverbed sediment using high-frequency acoustics: 1. Spectral properties of scattering, *J. Geophys. Res. Earth Surf.*, *119*, doi:10.1002/2014JF003189.

Received 23 APR 2014
Accepted 23 OCT 2014
Accepted article online 30 OCT 2014

Characterizing riverbed sediment using high-frequency acoustics: 1. Spectral properties of scattering

D. Buscombe[1], P. E. Grams[1], and M. A. Kaplinski[2]

[1]Grand Canyon Monitoring and Research Center, Southwest Biological Science Center, U.S. Geological Survey, Flagstaff, Arizona, USA, [2]School of Earth Sciences and Environmental Sustainability, Northern Arizona University, Flagstaff, Arizona, USA

Abstract Bed sediment classification using high-frequency hydroacoustic instruments is challenging when sediments are spatially heterogeneous, which is often the case in rivers. The use of acoustic backscatter to classify sediments is an attractive alternative to analysis of topography because it is potentially sensitive to grain scale roughness. Here a new method is presented which uses high-frequency acoustic backscatter from multibeam sonar to classify heterogeneous riverbed sediments by type (sand, gravel, and rock) continuously in space and at small spatial resolution. In this, the first of a pair of papers that examine the scattering signatures from a heterogeneous riverbed, methods are presented to construct spatially explicit maps of spectral properties from georeferenced point clouds of geometrically and radiometrically corrected echoes. Backscatter power spectra are computed to produce scale and amplitude metrics that collectively characterize the length scales of stochastic measures of riverbed scattering, termed "stochastic geometries." Backscatter aggregated over small spatial scales have spectra that obey a power law. This apparently self-affine behavior could instead arise from morphological scale and grain scale roughnesses over multiple overlapping scales or riverbed scattering being transitional between Rayleigh and geometric regimes. Relationships exist between stochastic geometries of backscatter and areas of rough and smooth sediments. However, no one parameter can uniquely characterize a particular substrate nor definitively separate the relative contributions of roughness and acoustic impedance (hardness). Combinations of spectral quantities do, however, have the potential to delineate riverbed sediment patchiness, in a data-driven approach comparing backscatter with bed sediment observations (which is the subject of part two of this manuscript).

1. Introduction

The use of swath mapping systems such as multibeam echo sounder (MBES) for measuring river bathymetry is on the increase because these systems can provide extensive coverage (hundreds to hundreds of thousands of square meters) in short periods (minutes to hours) [*Parsons et al.*, 2005; *Wright and Kaplinski*, 2011; *Guerrero and Lamberti*, 2011; *Grams et al.*, 2013]. High-frequency (several hundreds of kHz) MBES systems measure water depths (up to tens of meters) simultaneously along a wide swath perpendicular to the track of a moving vessel. High frequencies permit short acoustic pulse lengths (order microsecond or less) which, in combination with narrow along-track beam widths, allow high spatial resolutions (typically centimeters to meters). Since MBES systems are already used to map bathymetry, much attention has been paid to developing techniques that use the acoustic signals measured by the instrument to classify submerged sediment deposits by grain size [*Anderson et al.*, 2008; *Van Rein et al.*, 2009; *Snellen et al.*, 2013].

The basic premise behind acoustic sediment classification is that the magnitude of echoes measured by a MBES receive array depend, at least in part, on the composition of bed sediments, that have different backscattering properties due to impedance differences (acoustic hardness) and characteristic surface roughnesses [*Jackson and Richardson*, 2007]. Acoustic sediment classification techniques proposed to date are either statistical [*Amiri-Simkooei et al.*, 2009; *Eleftherakis et al.*, 2012; *Snellen et al.*, 2013] or based on physical models [*Jackeman*, 1988; *Lyons and Abraham*, 1999; *Snellen et al.*, 2013]. Statistical models are generally not able to separate the relative contributions of roughness and hardness in the backscatter signal. Currently, there is no widespread acceptance of any one particular technique [*Brown et al.*, 2011].

Classifications based on physical scattering models are currently limited to relatively deep water (several tens of meters or more) at low frequencies (up to 100 kHz) and moderate bed slopes (up to 10°)

[*Jackeman*, 1988]. Most physical models [e.g., *Matsumoto et al.*, 1993; *Fonseca et al.*, 2009; *Lamarche et al.*, 2011] are based on the variation of backscatter with the incidence angle made by the beam relative to the bed [*Jackson and Richardson*, 2007]. However, these models are relatively poorly developed for high frequencies [*Hellequin et al.*, 2003]. In addition, backscatter at large grazing angles (the angle made by an incident beam on a sloping bed) is both poorly modeled from an acoustics standpoint and generally agreed to be a poor sediment discriminator [*Jackson and Richardson*, 2007]. Heterogeneous riverbeds tend to form large slopes compared with typical shelf seafloors. Increases in slope increase the grazing angle for a given incident angle and therefore render sediment classification using angular dependence increasingly unsuitable. Rivers are typically shallow (up to tens of meters), which means small areas of the bed are insonified (the process of applying carefully controlled sound, usually for the purposes of measuring the response), leading to greater variation in backscatter amplitudes owing to small numbers of independent scatterers [*Amiri-Simkooei et al.*, 2009].

Techniques with a more general scope are predominantly statistical [*Brown et al.*, 2011] due to the stochastic nature of scattering by bed sediment and the nonuniqueness of a particular scattering amplitude [*Brown and Blondel*, 2009; *Brown et al.*, 2011], especially in shallow water [*Amiri-Simkooei et al.*, 2009] and the large variety in specifications of commercial multibeam systems [*Van Rein et al.*, 2009]. These statistical methods analyze the receive echo (backscatter) signals, aggregated over some scale, and relate them to observations of sediment type [*Shields*, 2010; *Snellen et al.*, 2013]. However, most of these methods to date are designed to be applicable over relatively large spatial scales (typically, several to hundreds of square meters of continental shelf seabed). The composition of riverbeds can be much more heterogeneous than typical shelf seabeds, in terms of typical length scales of patchiness (spatial persistence of different sediment types), the abruptness of sedimentary transitions, and the variety of covariation of bed forms with grain size over relatively short distances [e.g., *Dietrich and Smith*, 1984; *Paola and Seal*, 1995; *Nelson et al.*, 2009]. Sediment patchiness is a term often used to describe aggregations of bed sediment that are relatively homogeneous at the scale of 0.1–1 channel widths [*Nelson et al.*, 2014], although these patches can exist at all scales down to less than 1 m^2, which have been termed micropatches [*Vericat et al.*, 2008]. Sediment grain size between adjacent patches can vary by orders of magnitude over scales of meters.

There are three main considerations associated with this sediment heterogeneity. The first is that sediment varies considerably over the swath. Irrespective of the potential limitations associated with large slopes, angular backscatter relationships [*Fonseca et al.*, 2009], probably the most commonly employed sediment classification approach for seafloors [*Brown and Blondel*, 2009] can, by definition, only classify on a swath-by-swath basis thus assuming within-swath sediment homogeneity. In fact, the usable fraction of the swath is typically only half [*Hamilton and Parnum*, 2011]. Sediment in heterogeneous rivers tends to vary considerably over a typical swath width (tens of meters). Second, because backscatter must be considered at small spatial scales (ideally up to just a few meters), fewer spatially aggregated observations are amenable to classification approaches based on statistical models for backscatter distributions [*Amiri-Simkooei et al.*, 2009]. Third, high frequencies mean short (millimeter scale) acoustic wavelengths. When the bed can consist of combinations of silt, sand, gravel, cobble, and rock, scattering is transitional between acoustic regimes. For example, for a 400 kHz system with an acoustic wavelength of $\approx$3 mm (in fresh water), silt and sand are in the Rayleigh scattering regime (weak incoherent echoes) and gravel, cobble, and rock are in the geometric scattering regime (strong coherent echoes) [*Urick*, 1983]. This third consideration might actually help acoustic classification of riverbed sediment patchiness rather than hinder it.

The goal of this two-part manuscript is to identify signatures of small-scale (order meter) bed sediment patches in high-frequency backscatter from a heterogeneous riverbed. We adopt a phenomenological approach based on statistical analysis of backscatter. In departure from previously proposed methods, we use Fourier analyses to provide an objective, computationally efficient means by which to measure the spectral content (the strength of periodic components at different frequencies) of backscatter data. Previous research has examined the spectral properties of topographic data to gain insight into colocated backscatter, with an aim toward developing theoretical models for bed scattering [e.g., *Dziak et al.*, 1993; *Matsumoto et al.*, 1993; *Jackson et al.*, 1996; *Jackson and Richardson*, 2007]. Here we examine the spectral properties of backscatter toward a more pragmatic aim of empirically relating spectral parameters to sediment type for the purposes of sediment classification and, by extension, visualization of riverbed patchiness. Spectral analysis neither assumes nor requires a particular form of backscatter distribution (increasingly important as water depths decrease) and requires no knowledge of the physics of scattering by the bed. The great

advantage of spectral analysis to quantify the features of spatial fluctuations in backscatter (which are salient to variations in bed sediment type) is its ability to distinguish between signals with identical distributions but different autocorrelations. The problem is decomposed into two parts. In this part (Part 1), we

1. detail methods to correct raw high-frequency echoes recorded by the receive beams of a MBES in shallow water over a sloping heterogeneous riverbed for beam geometries (angle of sound incidence and area of beam of the sloping bed) and radiometries (source and transmission losses);
2. outline considerations for gridding georeferenced backscatter and derived metrics into digital surface models;
3. describe a general procedure to quantify the spectral characteristics (geometries) of gridded backscatter; and
4. develop a windowing procedure by which to construct spatially explicit maps of spectral properties that collectively quantify the length and amplitude scales of backscatter.

These maps can be estimated with the same spatial resolution as the input data and serve as the starting point for the second part [*Buscombe et al.*, 2014, hereinafter Part 2], which examines these spectral properties from areas of known sediment type, with a dual aim of examining the stochastic geometries of backscatter for individual sediment types and developing a rudimentary classification of riverbed sediment.

2. Methods

2.1. MBES Data Collection

For the purposes of this manuscript (Part 1), the methods described herein are illustrated using a single MBES data set collected from the Colorado River in Grand Canyon National Park, Arizona (at river mile 87 near Phantom Ranch, 140 km downstream from Lees Ferry, Arizona). The data consist of elevations and backscatter collected from an ≈1000 m by ≈100 m reach of riverbed. Many more data sets are analyzed and used in Part 2, with an identical processing chain as that described here. Details of backscatter collection, processing, and the field site are beyond the scope of the present manuscript but are described in detail in Part 2.

Data were collected using a 400 kHz Reson® 7125 multibeam sonar, which consists of emission and reception transducers with a monostatic Mills cross-arrays configuration that produces a swath comprised of 512 beams across a total across-track subtended angle of 135°. This geometry permits a swath width of up to 7 times the water depth. Each beam has a 0.5° across-track by 1.0° along-track angular width at half power (−3 dB). Each echo is registered simultaneously by all 512 beams, which constitute one ping. Pings are recorded up to 50 times per second. More details of sonar data collection are described in *Kaplinski et al.* [2009, 2014].

Sound velocity is measured at the sonar head, and periodically, casts of an acoustic sound velocity probe are taken through the water column (Figure 1). These profiles show that the water column is very well mixed (homogeneous): the sound velocity throughout water column is within 0.2 m s^{-1} of sound velocity measured at the surface (Figure 1). Ray-tracing corrections on the soundings are therefore not carried out. Long-term continuous measurements at gaging stations show salinity and temperature to be very slowly varying quantities.

2.2. Definitions and Assumptions

In this contribution we consider the (per beam, per ping) amplitude of backscattered sound associated with time-of-flight bathymetric sounding. The recorded amplitude is the integral of the portion of reflected sound at incidence angle from all scatterers in the insonified area of the bed (the beam footprint, Figure 2). The recorded amplitude is that associated with the range to the bed, which is either the peak amplitude or the amplitude associated with the highest phase coherence between the source sound wave and the echo. We do not distinguish between amplitudes from these two methods of bed detection.

Given the high frequency of the sound source, we assume that the acoustic penetration into the bed is negligible [*Jackson and Richardson*, 2007], and the effects of scattering by sediment volume heterogeneities are minimized [*Gallaudet and de Moustier*, 2003]. We therefore assume that the amplitude reflects the composition of bed surface sediment (and possibly form roughness within the beam footprint) only. Below, we use the term amplitude for the raw echo level recorded by the receive beams of the monostatic multibeam

Published 2014. American Geophysical Union.

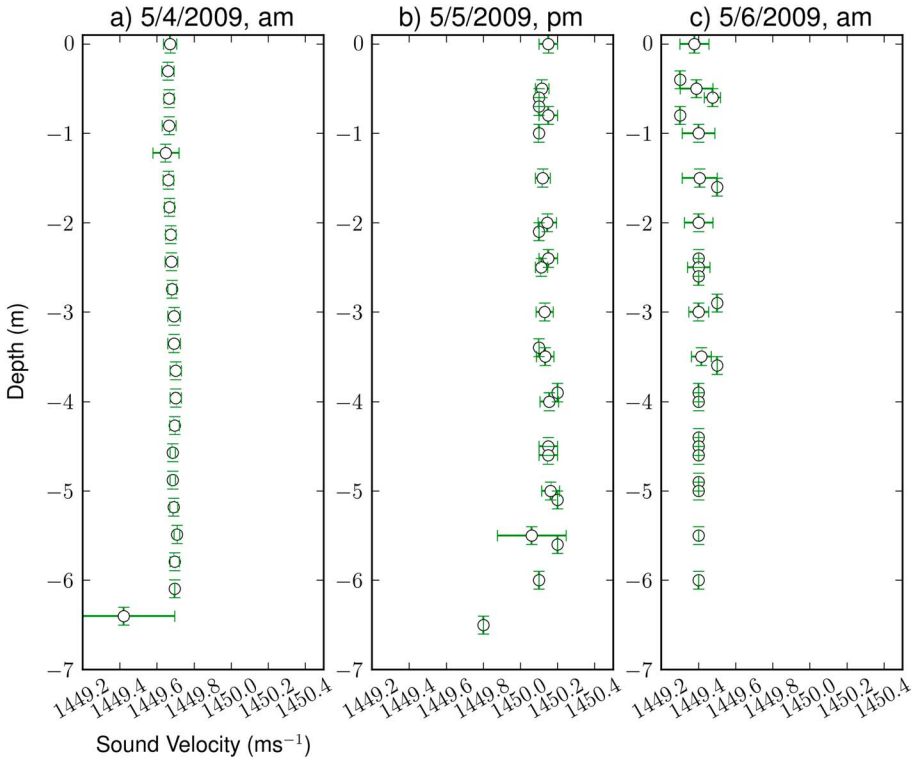

Figure 1. Profiles of sound velocity as a function of depth below the transducer, made on successive days at one survey site (river mile 30, in Marble Canyon, 48 km downstream from Lees Ferry), integrated over space. Error bars are 10 cm on the depth and 1 standard deviation (where multiple measurements per depth were made) on the sound velocity.

transducer and backscatter (which is really a backscatter coefficient because units remain relative—decibels (dB)—rather than absolute, i.e., pressure) for corrected amplitudes. The correction procedure is detailed in section 2.4.

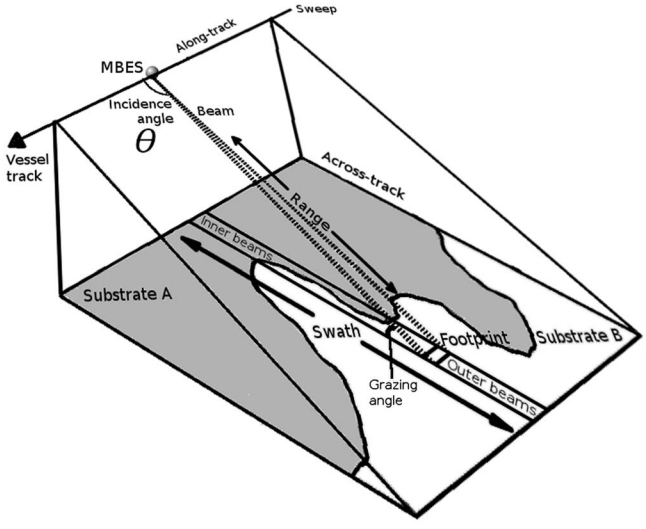

Figure 2. Terminology used describing a MBES receive geometry over a hypothetical heterogeneous riverbed on the order of a few square meters, during one sweep, at an instant in time (one ping). One swath, consisting of a number of beams, is highlighted that insonifies a narrow strip of the bed with varying sediment types (substrates A and B). For illustration, the geometry of just one beam is shown, with a small footprint.

2.3. Quality Control

Several checks are performed to ensure that only high-quality amplitude data are used for bed sediment characterization. Patch tests are conducted before initiating the surveys to determine the offset angles and timing between the various system components. Beam angle tests are used to determine the uncertainty of soundings for all beam angles [*U.S. Army Corps of Engineers*, 2004]. The procedure compares soundings for each beam angle to a reference surface. A reference surface is a digital elevation model (DEM) created for a portion of the riverbed using multiple overlapping sweeps with beam angles less than 45° (a 90° swath angle). A check line is collected over the reference surface with the full swath width, and the individual soundings from the check line are compared to the

Published 2014. American Geophysical Union.

reference surface to calculate the uncertainty of the soundings per beam angle. These tests show that the system is highly accurate, with uncertainty varying between 0.03 m and 0.05 m at the 95% significance level across all beam angles.

Quality assurance assessments are also performed in real time during the surveys by continuously monitoring across-track swaths and comparison between adjacent overlapping sweeps. A sweep is defined as the collection of pings made during one longitudinal passage of the boat (Figure 2). Several sweeps are required to map an entire pool of the river. Bad soundings and sweep misalignment can occur during high-rate vessel attitude changes (pitch, roll, yaw, etc.); through systematic side-lobe interference which affects successive pings; and scattering of soundings by air bubbles, drifting insects, and organic matter in the water; and the noisy acoustic environment. These soundings are identified by manual sweep editing and systematically stepping through overlapping sweeps. Judgments have to be made as to what soundings are usable: some groups of soundings are obviously outliers, yet others require an experienced eye to judge the quality of groups of soundings based on the range from the transducer and the context with the bathymetric surface as a whole [*Kaplinski et al.*, 2014]. For these reasons, surveys are conducted so there is always overlap between sweeps.

After manual filtering of soundings, an automated spatial filtering procedure is carried out, designed to identify artifacts based on (1) excessive bathymetric slopes and (2) beam locations. For each beam, if the bed slope in the along-track direction from the preceding beam to the present beam, and from the present beam to subsequent beam, both exceed 60°, and if the signs in slopes are opposite, then that beam is flagged. Along-track slopes are determined from the same beam in the previous and subsequent pings. Slopes $\geq$ 60° can occur (for example, rock faces), but at such high slopes, almost all of the sound is reflected specularly and the magnitude of the echo is poorly correlated with bed sediment composition [*Jackson and Richardson*, 2007]. In addition, a sounding is flagged if groups of outer beams have smaller across-track distances than inner beams. These are identified as beams whose footprint on the bed is more than 2 m inboard of an inner beam. These beams are therefore unreliably positioned. One could go further by flagging (or filtering) beams with excessive spatial gradients in backscatter. However, we have no physical (or acoustic) basis upon which to define a threshold to do this. All amplitudes and depths associated with flagged beams are not considered further.

2.4. Geometric and Radiometric Corrections

Angle-induced biases in amplitude, considered an inherent property of swath sonar bed scattering [*Jackson*, 1994] are corrected for each beam. This process minimizes the sensitivity of backscatter to system calibration [*Snellen et al.*, 2013]. As the ratio of instantaneous insonified area to the nonnadir beam footprint reduces with increasing beam grazing angle (the angle made by an incident beam on the sloping bed), the number of time samples also increases and amplitudes therefore have an angular dependence [*Simons and Snellen*, 2009]. In addition, the relative contribution of specular reflections and volume scattering also decrease with grazing angle.

Amplitudes are corrected for variation with grazing angle as follows. The average amplitude as a function of the grazing angle with the bed is computed for 1° spaced bins extending the full swath, port, and starboard. Grazing angles are computed by factoring in the across-track bed slope. For grazing angles > 15°, the plane fitting extends over the two adjacent bins (i.e., three bins used for each angular value). Averages are made over 50 consecutive pings for stable estimates of the angular mean. Amplitudes are recorded in dB, so corrections are subtracted from the raw values and then a reference value taken at a reference angle of 30° (from nadir) is added back in. This is a standard approach based on the assumption that the reference angle is minimally sensitive to slope correction and absorption errors, and is usually in the region 30–50° [*Jackson*, 1994; *Kloser et al.*, 2010].

Backscatter, $B(\theta)$ (dB), is calculated by balancing the following acoustic budget for the system [*Urick*, 1983; *Amiri-Simkooei et al.*, 2009]:

$$B(\theta) = \mathrm{EL}(\theta) - \mathrm{SL} + 2\mathrm{TL}(\theta) - 10\ \log\left[A_f(\theta)\right] \tag{1}$$

where echo level $\mathrm{EL}(\theta)$ (dB) is the received amplitude after correction due to angular effects; SL is the (measured) time-varying source level (dB), which is a function of the transducer-array beam pattern and is

proportional to the transmit power steering. Transmission loss, TL (dB), is estimated using [*Le Gonidec et al.*, 2003]

$$\mathrm{TL} = \left(2\epsilon_s + 2\epsilon\right) R + 40\ \log\left(R\right) \tag{2}$$

where $R{=}d/\cos\left(\theta\right)$ is the range (m); d (positive down) is the water depth below the transducer (m); ϵ_s and ϵ are attenuation due to sediment and water (Appendix A), respectively. These simple corrections for sediment are appropriate for relatively small concentrations (up to about 1 g/L) of fines (silt and clay), which are homogeneously suspended in the water column. The acoustic footprint $A_f(\theta)$ is calculated for $\theta \neq 0$ as [*Simons and Snellen*, 2009; *Amiri-Simkooei et al.*, 2009]

$$A_f(\theta) = \frac{c\mathrm{TR}\Omega_{\mathbf{x}}}{2\ \sin\left(\theta - \beta_{\mathbf{y}}\right)\ \cos\ \beta_{\mathbf{x}}} \tag{3}$$

where $\beta_{\mathbf{x}}$ and $\beta_{\mathbf{y}}$ are respectively the riverbed slopes in the along-track and across-track directions; T is the transmit pulse duration (s); c is the speed of sound in water (m s^{-1}), and $\Omega_{\mathbf{x}}$ is the along-track beam aperture. At high grazing angle where $\theta \approx 0$, equation (3) reduces to the flat bed case: $A_f(\theta = 0) = R^2\Omega_{\mathbf{x}}\Omega_{\mathbf{y}}$ [*Simons and Snellen*, 2009]. Automated quality control, grazing angle corrections, and slope estimations for beam footprint calculations are carried out using MB-System software [*Caress and Chayes*, 1996, 2014].

2.5. Gridding

Geometrically and radiometrically corrected georeferenced backscatter data are mapped onto a regular grid using spline-under-tension continuous curvature interpolation [*Smith and Wessel*, 1990]. This bicubic spline technique produces an analytical solution for the surface $B(\mathbf{X})$, where coordinate vector $\mathbf{X}$ ranges over a two-dimensional domain $[X, Y]$, obtained by solving:

$$(1-\kappa)\nabla\left[\nabla(B(\mathbf{X}))\right] + \kappa\nabla\left[B(\mathbf{X})\right] = 0 \tag{4}$$

where κ is a tension factor between 0 and 1, and ∇ indicates the Laplacian operator. $\kappa > 0$ minimizes undesired oscillations and false local maxima or minima [*Smith and Wessel*, 1990]. This approach is preferable to Delaunay triangulation due to enhanced computational efficiency on these very large data sets (millions of data points per variable per survey) and, under tension, it is less prone to error at abrupt changes. Following *Smith and Wessel* [1990], we use $\kappa = 0.35$ because the field of backscatter is a rapidly varying quantity with steep spatial gradients.

Suitable values for quantity $B(\mathbf{X})$ can be any measure of central tendency in the distribution of values in a cell, or a percentile of the cumulative distribution. These quantities, as well as optimal grid size, are discussed in Part 2.

2.6. Power Spectra

We consider $B(\mathbf{X})$ as a random field specified by the joint probability density function $p(B(\mathbf{X}_1), B(\mathbf{X}_2), \ldots : \mathbf{X}_1, \mathbf{X}_2, \ldots \in [X, Y])$. The use of Fourier methods to make useful measurements from quasi-periodic, yet non-sinusoidal, data has a long history [*Priestley*, 1981]. The discrete Fourier transform (DFT) of $B(\mathbf{X})$ consisting of $N_X \times N_Y$ observations at regular intervals $\Delta X = \Delta Y$ is as follows [*Priestley*, 1981]:

$$W_2(\mathbf{K}) = \sum_{m=0}^{N_X-1}\sum_{n=0}^{N_Y-1} B(m\Delta X, n\Delta Y)e^{-2\pi i\left(\frac{k_X m}{N_X} + \frac{k_Y n}{N_Y}\right)} \tag{5}$$

where i is the imaginary unit, e is the base of the natural logarithm, m and n are increments in X and Y, respectively, and $\mathbf{K}{=}(k_X, k_Y)$ is a two-dimensional wave vector (whose magnitude $K{=}\sqrt{k_X^2 + k_Y^2}$ is the wave number) related to the frequency components by $F_X = \frac{k_X}{N_X\Delta X}$ and $F_Y = \frac{k_Y}{N_Y\Delta Y}$. Therefore, the wave number is the number of times the function $B(\mathbf{X})$ has the same phase per unit space. Subscript 2 in equation (5) (and elsewhere below) denotes that this is a 2-D operation. The power spectrum, a measure of the variance in $B(\mathbf{X})$ associated with different narrow bands of frequency, is estimated using the periodogram of equation (5), which has units dB^2:

$$P_2(\mathbf{K}) = \frac{1}{N_X^2 N_Y^2}|W_2(\mathbf{K})|^2 \tag{6}$$

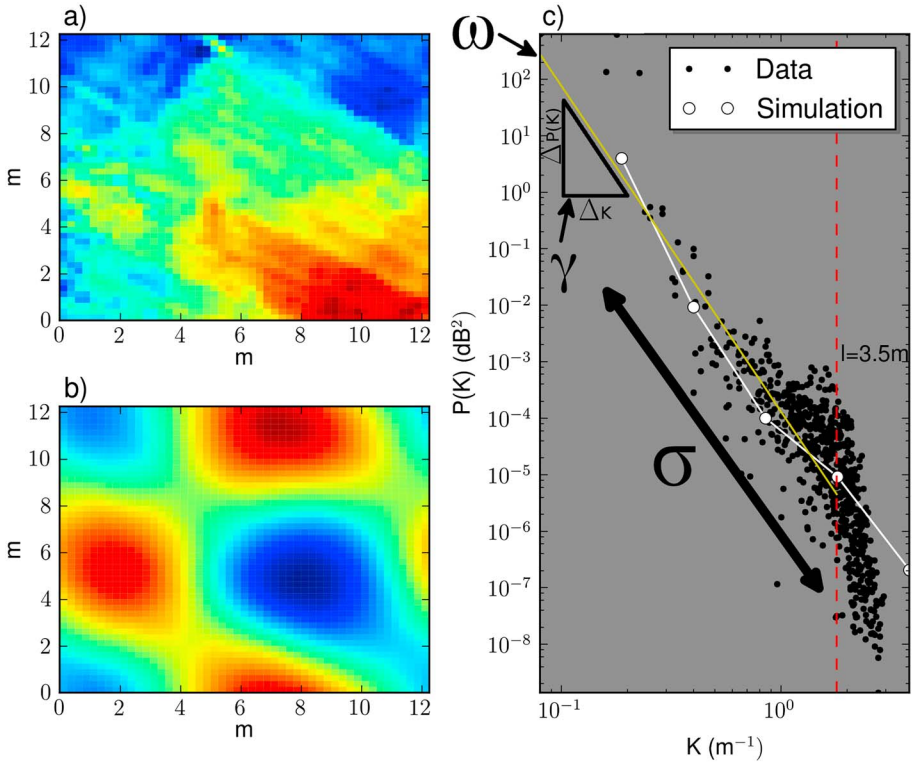

Figure 3. Example of spectral processing: (a) a 12.5 m^2 patch of gridded backscatter (50 × 50 grid cells of 0.25 × 0.25 m); (b) the 2-D random field simulated from the power spectrum of detrended and Hann-tapered (Figure 3a); (c) the marginal power spectrum of the backscatter data (black dots) and the bin-averaged spectrum of the simulated field (white dots). Note that the simulation in Figure 3b is not intended to mimic the spatial pattern of the data in Figure 3a, only the dominant spectral content. The outer length scale, *l*, is shown by the vertical dashed red line, corresponding to a scale of 3.5 m (in this example), calculated based on the divergence from the marginal spectrum. Wavelengths smaller than this are not considered for the linear least squares fit through the data (yellow line), from which the spectral strength (ω_1) and exponent (γ_1) parameters are defined.

To prevent spectral leakage, equation (6) is calculated by (1) detrending the data by a linear least squares 2-D plane and (2) applying a Hann taper, normalized to account for the change in variance associated with its application, such that equation (6) becomes [*Perron et al.*, 2008]:

$$P_2(\mathbf{K}) = \left(N_X^2 N_Y^2 \sum_{m=0}^{N_X-1} \sum_{n=0}^{N_y-1} H(m,n)^2 \right)^{-1} |W_2(\mathbf{K})|^2 \tag{7}$$

The 1-D marginal spectrum, $P_1(\mathbf{F})$, is the 2-D spectrum (equation (7)) collapsed as a function of the radial frequency $\mathbf{F} = \sqrt{F_X^2 + F_Y^2}$ (Figure 3). The subscript 1 here, and elsewhere below, denotes calculations based on the 1-D form of the spectrum. No radial integration occurs; therefore, this spectral form incorporates any anisotropy in $B(\mathbf{X})$.

2.7. Stochastic Geometries

Four useful quantities calculated from $P_1(F)$ (Figure 3) are the spectral strength (ω_1), the spectral exponent (γ_1), the integral length-scale (l_0), and the variance in amplitude (σ_1^2). We term these quantities stochastic geometries, in the sense of *Fara and Scheidegger* [1961], because they are statistical measures of physical amplitude and length scales and also because the units of these scales are mixed. The spectral strength is a measure of power at low frequencies. The spectral exponent is a measure of the rate of decay in power as a function of increasing frequency. The integral length scale is a measure of the persistence (autocorrelation) in the data. The amplitude variance is calculated over all resolvable (and statistically significant) scales. The remainder of this section details how these quantities are calculated.

Spectral power decreases rapidly with increasing frequency. A simple functional form of $P_1(F)$ is a power law [*Jackson and Richardson*, 2007]:

$$\widehat{P_1(\mathbf{F})} = \frac{\omega_1}{(h_0|\mathbf{F}|)^{\gamma_1}}, \qquad |\mathbf{F}| > 1/l \tag{8}$$

where l defines the outer length scale of the spectrum. The inclusion of a dimensional constant, h_0, in equation (8) allows ω_1 to have dimensions dB^2, independent of the value of γ_1 [*Jackson and Richardson*, 2007]. This power law behavior cannot persist at very high frequencies, which lead to a phenomenon known as spectral roll over where the spectral slope steepens [*Priestley*, 1981]. The length scale associated with this rollover frequency is the outer scale l, which is calculated as the point of divergence between $P_1(\mathbf{F})$ and a background power spectrum [*Perron et al.*, 2008].

The background spectrum is required to calculate l but is also useful to identify noise at high frequencies and assess the significance of the spectrum (detailed below). This background spectrum, $\overline{P_2(\mathbf{K})}$, is calculated from a simulated Gaussian 2-D random field drawn from $P_2(\mathbf{K})$ using the methods detailed in *Oppermann et al.* [2013] and *Selig et al.* [2013]. This approach preserves the same covariance of the simulated field as the data. The obtained simulation is statistically homogeneous and isotropic, which means that the correlation between two field values at position $\mathbf{X}$ depends only on their physical distance ($|\mathbf{X}_1 - \mathbf{X}_2| \propto 1/\mathbf{K}$). It is therefore a smooth spectral approximation to an isotropic form of $P_2(\mathbf{K})$. The spectra of $B(\mathbf{X})$ and a Gaussian field with the same covariance function remain similar over a large number of low frequencies because the covariance captures the essential features of variation of backscatter over relatively large separation distances. The divergence appears at high frequencies because it cannot represent either large changes in amplitude over short distances [*Sayles and Thomas*, 1978] or asymmetry about a vertical or horizontal axis, because it is unaffected by a change in sign of $\mathbf{B}_1$-$\mathbf{B}_2$ or $\mathbf{X}_1$-$\mathbf{X}_2$ [*Goff and Jordan*, 1988]. Background spectra are calculated in 2-D then collapsed as a function of $\mathbf{F}$ to give $\overline{P_1(\mathbf{K})}$.

Spectral strength and exponent are estimated from bin averages of the marginal power spectrum $P_1(\mathbf{F})$, as the parameters that minimize the error:

$$|| \left(\gamma_1 \mathbf{F}_b + \omega_1\right) + \widehat{P_{1b}} ||^2, \qquad |\mathbf{F}| > 1/l \tag{9}$$

where $||$ represents the two norms; $\widehat{P_{1b}} = \log 10[P_1(\mathbf{F}_b)]$ and $\mathbf{F}_b$ denote b linearly spaced bins of $\log 10[\mathbf{F}]$ up to the frequency associated with l. The parameter vector $(\gamma_1, \omega_1)^t$, where t indicates transpose, is the least squares solution of the following overdetermined linear system:

$$\begin{bmatrix} \mathbf{F}_1 & 0 \\ \mathbf{F}_2 & 0 \\ \vdots & \\ \mathbf{F}_b & 0 \end{bmatrix} (\gamma_1, \omega_1)^t = \begin{bmatrix} \widehat{P_{11}} \\ \widehat{P_{12}} \\ \vdots \\ \widehat{P_{1b}} \end{bmatrix} \tag{10}$$

The spectral power corresponding to a confidence level $\alpha = 0.05$ is calculated using the χ^2 cumulative distribution function [*Gilman et al.*, 1963; *Torrence and Compo*, 1998]:

$$P_{1_\alpha}(\mathbf{F}) = \frac{1}{2}\chi_2^2(1-\alpha)\overline{P_1(\mathbf{F})} \tag{11}$$

where subscript 2 on χ^2 refers to the degrees of freedom [*Jenkins and Watts*, 1968]. Only the $P_1(\mathbf{F}) > P_{1_\alpha}(\mathbf{F})$ are used to fit the regression using equation (10) (Figure 3). Usually the regression is fit to only a subset (up to approximately half) of the original spectrum due to these tests of statistical significance.

The autocovariance function $\xi_1(L)$, over L lags, is calculated as the 2-D continuous Fourier transform of $P_2(\mathbf{K})$ [*Priestley*, 1981] then integrated radially over segments to collapse it to 1-D:

$$\xi(L) = \int_0^{2\pi} \left(\int_{-\infty}^{+\infty} P_2(\mathbf{K}) e^{-i\mathbf{K}L} \mathrm{d}L \right) (\mathbf{K}\cos\psi, \mathbf{K}\sin\psi)\mathbf{K}\mathrm{d}\psi \tag{12}$$

where ψ is a vector of angles over which the radial integration occurs. The assumption here is that the radial integration incorporates any significant anisotropy in $B(\mathbf{X})$. The integral length scale, l_0, is defined as the product of 2π and the lag at which ξ_1 falls to half its value at zero lag [*Taylor*, 1938]. Finally, the area under the power spectral density curve is the variance of the amplitude distribution [*Sayles and Thomas*,

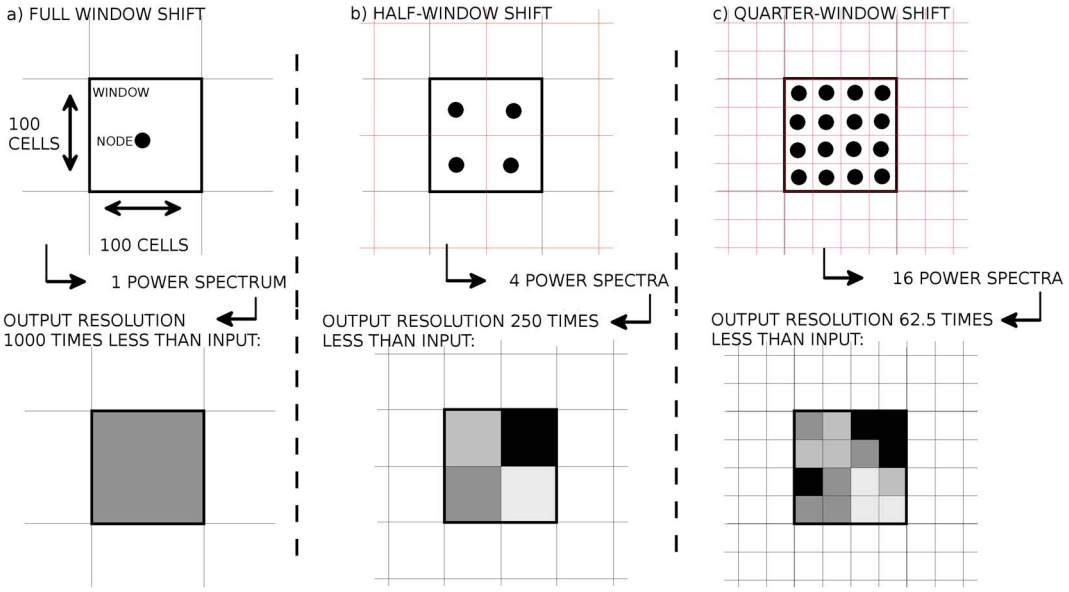

Figure 4. Schematic of the windowing procedure to create spatially explicit maps of stochastic geometries. In each case, inputs are 100 × 100 grid cells. Three idealized cases are shown: (a) full-window shift (0% overlap), (b) half-window shift (50% overlap), and (c) quarter-window shift (75% overlap) on the same window (size and position). Shifts occur in the vertical and the horizontal. For each shift a node is created in the center of the shifted window. The spectrum is calculated for the shifted window and the values of stochastic geometries assigned at the node location. The output resolution in Figure 4a is 1/1000 that of the input, and the output resolutions in Figures 4b and 4c are 4/1000 and 16/1000 that of the input, respectively.

1978]. The DFT periodogram power spectrum estimate (dB^2) is linearly related to power spectral density (dB^4), therefore,

$$\sigma_1^2 = 2\sqrt{\int_{\mathbf{F}_0} P_1(\mathbf{F})d\mathbf{F}}, \qquad \mathbf{F}_0 = |\mathbf{F}| > 1/l \tag{13}$$

in which the definite integral is estimated using the trapezoidal method on the statistically significant portion of $P_1(\mathbf{F})$ ($P_1(\mathbf{F}) > P_{1_\alpha}(\mathbf{F})$). The factor of 2 in equation (13) accounts for the symmetry in the DFT array. For normally distributed amplitudes, the square root of equation (13), σ_1, is equivalent to the root-mean-square backscatter (dB). Drawing parallel with the usage of the same metric to describe roughness of elevation surfaces [*Sayles and Thomas*, 1978], and because backscatter amplitudes are not usually normally distributed, especially in shallow water [*Amiri-Simkooei et al.*, 2009], we refer to this quantity simply as acoustic roughness, which does not pertain to any particular distributional form.

Complex spatial patterns of backscatter must be described by a range of frequencies, so the spectral exponent, γ_1, which quantifies the rate of decay in power as a function of frequency, is a useful measure of how complex the data is by quantifying the range of frequencies necessary to describe the data (spectral width). Spectral strength, ω_1, and roughness, σ_1, both measures of the amplitude of spectral power, are useful measures of the magnitude of backscatter fluctuations over space. The spectral strength, ω_1, quantifies the extent to which the spectrum becomes red-shifted by decreases in spectral width. Parseval's theorem states that the sum of the spectrum must equal the variance in the data; therefore, steep gradients in the spectrum dictate intercepts at large power: when backscatter has large variance at low frequencies, ω_1 is large. Roughness is a scalar that describes the overall power in the spectrum over all frequencies or the spatial variability of backscatter over the window. This quantity can be shown to be scale dependent [*Sayles and Thomas*, 1978; *Hough*, 1989] and therefore may only be a meaningful metric when comparisons are made of spatially explicit spectral maps with the same resolution. Integral length scale, l_0, is a measure of the largest statistically significant scale in the power spectrum, describing the length scale over which the surface is typically statistically similar, characterizing the scale of the large, low-frequency fluctuations in the data.

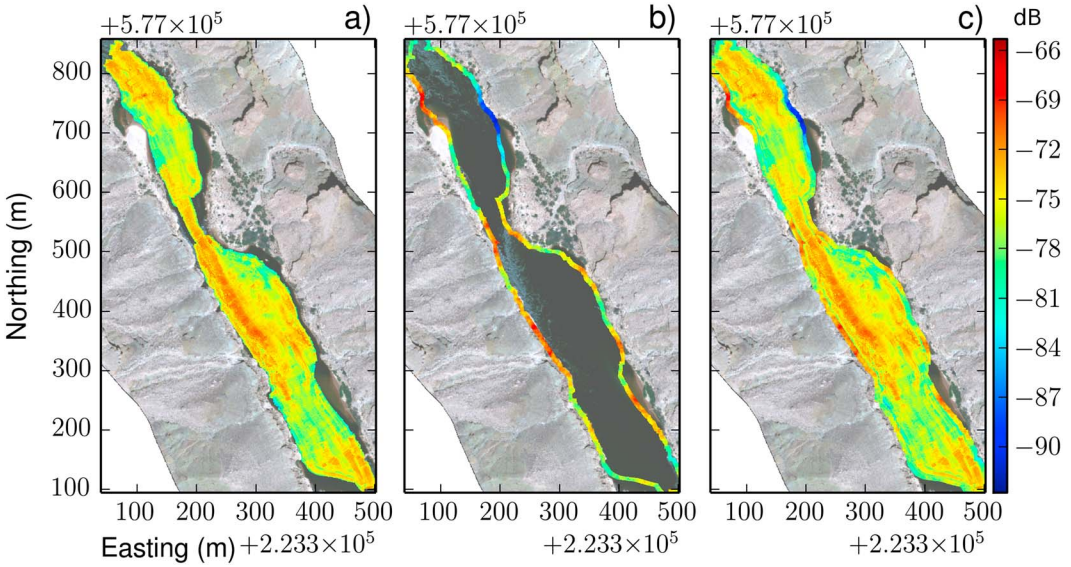

Figure 5. Example spectral padding procedure to minimize edge effects in the windowed spectral processing: (a) median backscatter data gridded in 0.25 × 0.25 m cells; (b) simulated data, with the same spectral properties as Figure 5a, to pad beyond the boundaries of Figure 5a; and (c) the padded data for analysis. Large backscatter values are hot colors.

2.8. Spatially Explicit Spectral Maps

In this section we describe a procedure to create spatially explicit maps of ω_1, γ_1, σ_1, and l_0, the quantities collectively describing the stochastic geometry of backscatter, detailed in section 2.7, from the digital surface model $B(\mathbf{X})$. These spectral maps show in detail the spatial heterogeneity of the variation in spectral frequency content and amplitude.

For each of the four stochastic geometries, g, the procedure consists of three stages: (1) spectral padding, (2) creating overlapping square windows of $B(\mathbf{X})$ and calculating g for a set of nodes defined for each window, and (3) creating a new surface of g at those nodes. With reference to Figure 4a, a window is a fixed frame of reference: a square area composed of several grid cells. For illustration, the single window in each of the three examples in Figures 4a through 4c is identical in area and position and composed of 100 × 100 grid cells. If the degree of overlap is 0% the window is shifted a full length in the horizontal and vertical directions. For each shift, a spectrum is calculated according to the methods detailed in section 2.6, and for each spectrum the four stochastic geometries are computed according to the methods detailed in section 2.7. The node positions within the window depend on the number of shifts, for example, a half-window shift (overlap of 50%) creates four nodes because the shift is applied in both the horizontal and vertical dimensions (Figure 4b) and a quarter-window shift creates 16 nodes (Figure 4b).

In order to achieve a resolution identical to the input, the shift is 1 grid cell, so as many nodes as there are cells are assigned values from the spectral processing. For the 100 × 100 window in Figure 4 this would be 10,000 individual nodes and computed spectra. The technique is computationally demanding: 10 million spectra must be computed for a data set comprised of 1000, 100 × 100 cell windows, with one-grid shifts. However, the problem is readily amenable to both parallel and distributed computing because the inputs (a small window of the data, typically 10,000–100,000 grid cells) and outputs (essentially, four numbers: ω_1, γ_1, σ_1, and l_0) are small in size for each window/shift. The full-resolution operation on the map of backscatter depicted in Figure 5c, using parallel processing running code implementations written in an interpreted language (Python/Cython), completes in minutes (on a four-core 2.8 GHz, ≈8 MB cache processor).

Given the irregular shape of the surveyed area, in a window on the edge of $B(\mathbf{X})$, many grid cells might be empty of data. Therefore, empty cells in boundary windows, as well as all cells in one adjacent window are filled with artificial data which have the same statistical properties as the portion of the window which is filled with data. This procedure is common in spectral analysis and is termed "padding." Its purpose is to eliminate edge (boundary) effects in the windowing procedure, in order to produce statistically reliable values of the stochastic geometries in the outermost grid cell. Padding is achieved by filling each empty

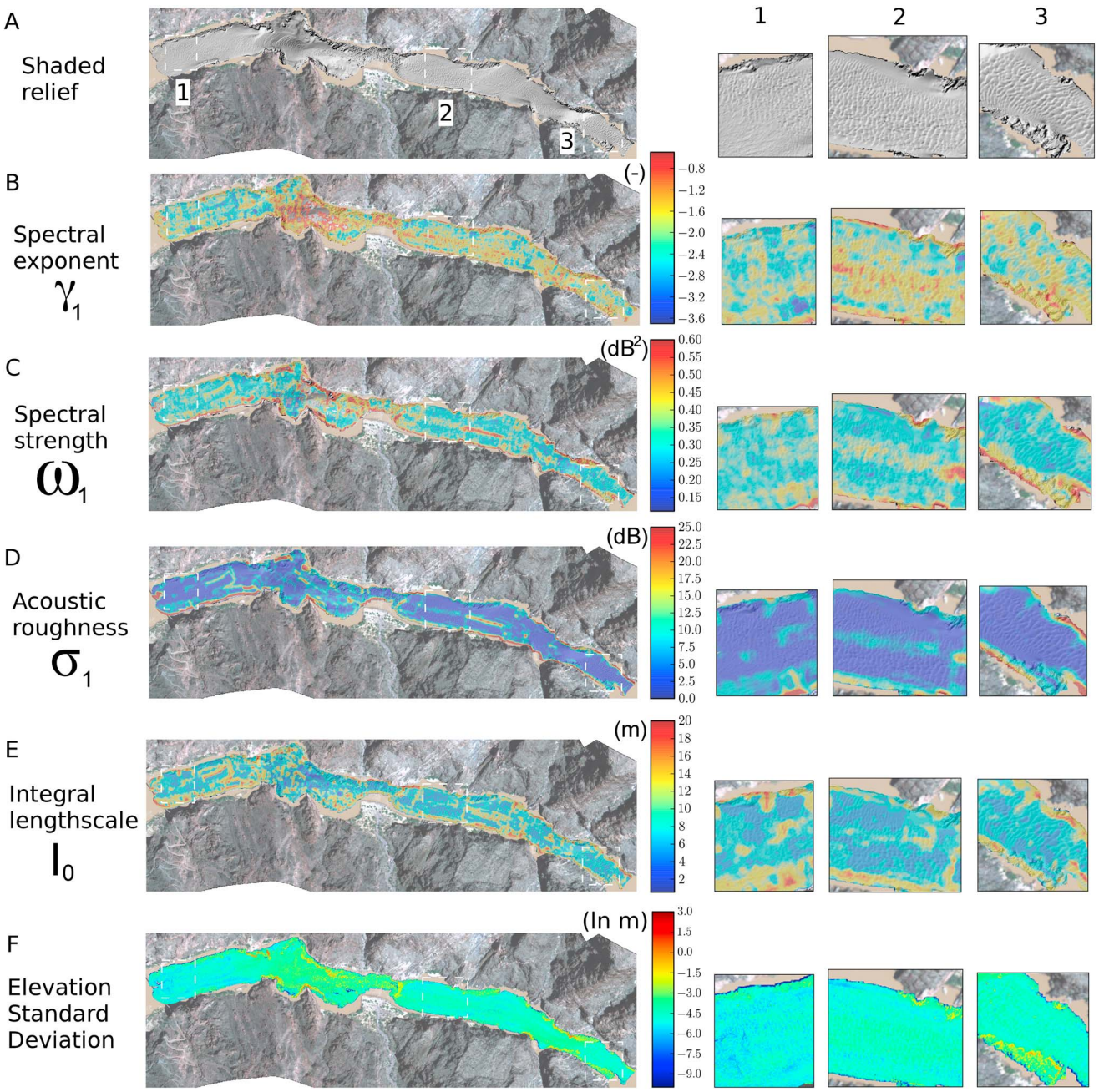

Figure 6. Maps of (a) shaded relief, (b) spectral exponent, γ_1 (nondimensional) (c) spectral strength, ω_1 (dB^2), (d) acoustic roughness, σ_1 (dB), (e) integral length scale, l_0 (m), and f) per-grid standard deviation in elevations, log scaled to accentuate the spatial pattern, at river mile 87 (in Grand Canyon, 140 km downstream from Lees Ferry). Three areas with rhythmic within-channel morphology have been identified as 1, 2, and 3, which are shown to the right of each subpanel at a scale of 300%.

grid cell with a realization of a Gaussian random field with the same spectrum as $B(\mathbf{X})$ Figure 5). These random field values are estimated using exactly the same procedures used for calculating background spectra for individual windows, as detailed in section 2.7. Upon completion of the creation of the new surface, the padding cells are removed: their purpose is simply to help estimate a reliable stochastic geometry in the boundary cells that may (or may not) have missing data.

3. Results

A digital surface model of median backscatter $B(\mathbf{X})$, gridded at 0.25 × 0.25 m, was constructed and analyzed using the methods detailed in section 2.8 using a window size of 100 × 100 grids (25×25 m), and a step size

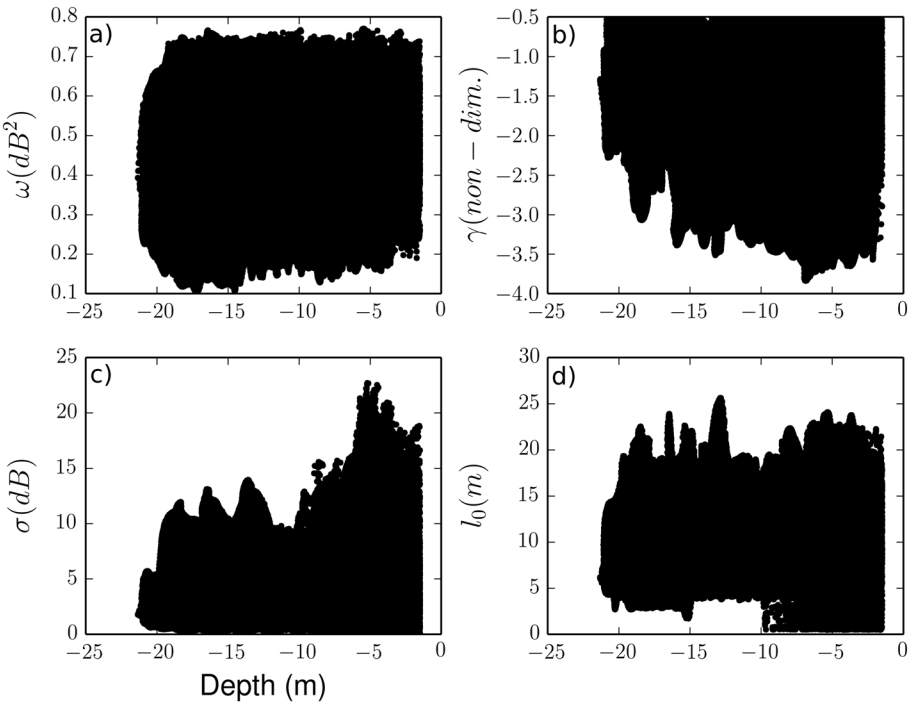

Figure 7. The (lack of) relationship between water depth and (a) spectral strength, ω_1 (dB^2), (b) spectral exponent, γ_1 (nondimensional), (c) acoustic roughness, σ_1 (dB), and (d) integral length scale, l_0 (m), for the data at river mile 87 (in Grand Canyon, 140 km downstream from Lees Ferry).

of one grid (0.25 m). The resulting four maps of spectral strength, spectral exponent, integral length scale, and roughness (Figures 6b through 6e), therefore, preserve details at a resolution of 0.25 × 0.25 m. The grid size was chosen as the smallest scale at which there were multiple usable soundings after quality control procedures. To aid interpretation and discussion of the spatial patterns revealed in the maps of stochastic geometries, maps of the shaded relief (Figure 6a) and per-grid standard deviation of elevations (log scaled, Figure 6f), which is frequently used as a roughness indicator from topographic data, are also presented.

The area marked 1 in Figure 6 has an abrupt transition from rhythmic morphology on river right to non-rhythmic morphology on river left. The other two areas (marked 2 and 3) are characterized by dune morphologies with differing geometries. It is instructive to examine how spatial variability of these stochastic geometries varies with small- to medium-scale morphologies. Each of these parameters are uncorrelated with depth (Figure 7); however, shaded relief maps (gridded at the same resolution) are a powerful means with which to scrutinize spectral geometries with morphological features such as low- and high-amplitude dunes, boulders, rock ledges, and planar beds readily apparent (Figure 6a). Each spectral quantity is typified by variability over scales of up to tens of meters, illustrated by close-up details of three areas (denoted 1, 2, and 3 in Figure 6), which are approximately equal to changes over several hundreds of meters.

Three areas in Figure 6 have been highlighted because of their quite distinctive morphologies. First, the close-up detail in area 1 of Figure 6 shows a short reach with an abrupt transition from low-amplitude rhythmic morphology to what appears to be a more planar bed with coarse substrate. The sedimentology of this area shows no abrupt transition, however. The dune field is composed of sand and gravel, and the adjacent cobble bar is filled with varying quantities of sand. While highly variable, values of σ_1 and l_0 are generally larger on the planar side of the transition. The same pattern is evident in both ω_1, γ_1, although somewhat muted. The abrupt transition in the morphology of area 1 is not reflected in the spectral parameters, which suggest that they are more sensitive to the sedimentology of the area than to the morphology.

Second, the close-up detail in area 2 of Figure 6 shows a short reach dominated by dunes with a more three-dimensional structure and greater spatial variability. From the shaded relief maps it is clear that there are features with rhythmic morphology; however, the crests are both lower in amplitude and less linear than in area 1. The dominant patterns in ω_1, γ_1, σ_1, and l_0 trend longitudinally, i.e., perpendicular to the

orientation of the bed form crests. In particular, the ridge of high values in each of the four stochastic geometries trends toward the center of the channel. There are no abrupt changes in depth; indeed, this section of the channel is relatively flat. The variation is due to individual small boulders in the dune field which are barely visible in the hill-shaded bathymetry.

Finally, the close-up detail in area 3 of Figure 6 shows a short reach of approximately linear and steep sand dunes flanked by rocks in shallow areas either side, visible in the shaded relief map (Figure 6a). The large-scale pattern is the high values of each parameter over the rocky areas and the low values in the sandy regions. Qualitatively, it makes physical sense that variance in backscatter (σ_1) would be low over physically more smooth surfaces (the roughness signal) and spectral slope, and intercept (ω_1 and γ_1, respectively) would also be low over sandy surfaces with lower acoustic impedance (the hardness signal). While the present method, in common with other phenomenological approaches based on backscatter statistics, cannot separate the relative contributions of roughness and hardness, the use of spectra does at least allow roughness length scales to be quantified, which significantly aids physical interpretation. There is little variance in σ_1 across the sand dune field; however, there are patches of that field with significantly different values of ω_1, γ_1, and I_0, which implies some variability in surface roughness and/or hardness. This could be due to topographic or grain size variations or both.

4. Discussion

In general and qualitative terms, areas of rocks and boulders (rough and hard) are associated with relatively high values of all four stochastic geometries. Areas of relatively soft materials (dune-forming sands and gravels) have relatively low values. For the 400 kHz instrument used here, sands are in the Rayleigh scattering regime but small proportions of small gravels would make the sediment transitional between Rayleigh and geometric regimes. Areas of coarse-grained but relatively planar bed have a range of values of all four stochastic geometries, so the signature is indeterminate. The coherence of the scattering (Rayleigh or geometric) caused by either acoustic frequency or varying proportions of gravel in the mixture could affect the distribution of backscatter magnitudes enough to make discrimination between sands and gravels indeterminate. It is therefore more likely that combinations of these parameters would be required to uniquely characterize a particular substrate or separate the relative contributions of surface roughness and acoustic impedance. An evaluation of the validity of this hypothesis, for heterogeneous riverbeds, requires spatially explicit maps of these quantities at high resolution in order to have the density of observations with which to compare with bathymetric features and sediment observations (which is the subject of Part 2) at the same resolution.

Spectra of surfaces of backscatter obey a power law form because there is no significant concentration of spectral power in any particular frequency band, indicative of a continuum of wavelengths of backscatter, just as morphology and grain size have a continuum of wavelengths. Backscatter, like morphologies [*Nikora et al.*, 1998; *Perron et al.*, 2008], are generally larger in amplitude at longer wavelengths. Modeling backscatter spectra using an inverse power law: $\widehat{P_1(\mathbf{F})} \propto \mathbf{F}^{\gamma_1}$ (equation (8)), values of γ_1 tend to vary between −0.5 and −3.5 (Figure 6a) that implies that the scaling relationship between amplitude and wavelength does not hold over all wavelengths. In the terminology of fractals, backscatter surfaces are self affine [e.g., *Voss*, 1988; *Turcotte*, 1997]. If this is indeed the case, $\gamma_1 < -3$ would indicate that shorter-wavelength fluctuations in backscatter have larger amplitude-to-length ratios, which would in turn indicate that scattering is high magnitude but not spatially persistent. Rocks and boulders (in Figure 6a) are found to have higher γ_1 compared to relatively smooth dune surfaces. For a self-affine surface, this would indicate that the rate at which backscatter amplitude declines relative to wavelength is smaller for hard, rough surfaces compared with relatively smooth and soft surfaces. This seemingly physically nonintuitive result prompts us to suggest that the power law behavior is instead indicative of multiple processes operating over multiple overlapping scales [e.g., *Hough*, 1989; *Jackson and Richardson*, 2007]. For example, the influence of form roughness (ripples, and dunes) on acoustic scattering; this may be qualitatively consistent with a simple conceptual model for the heterogeneous riverbed where the backscatter signal is indicating a continuum of changes in bed sediment grain size over discrete morphological units, or a situation where sediment and backscatter are more rapidly varying quantities, superimposed over slower changes in surface topography.

Collectively, the above would indicate that relating the stochastic geometries of backscatter to surface sediment type is feasible if the following conditions are met:

1. The stochastic geometry of backscatter is defined at a resolution, and over a window, small compared to the length scale over which significant changes in the geometries of local morphological forms occur, in order to maximize the likelihood that the grain size signal is captured independent of the morphological signal.
2. This small window is sufficient in size to aggregate enough observations to provide a statistically meaningful measure.
3. Some measure or combination of measures of stochastic geometry of backscatter are able to tease out the relative contributions of roughness and acoustic impedance (hardness), if these quantities do not scale with grain size.

These issues are addressed in Part 2.

5. Conclusion

Methods have been presented to construct spatially explicit maps of spectral properties from georeferenced point clouds of geometrically and radiometrically corrected echoes from a high-frequency multibeam echo-sounder (MBES). There are three stages to this process. First, a digital surface model of an appropriate parameter of the distribution of backscatter in a defined area (grid size) is created using a gridding algorithm that is relatively insensitive to, and captures the essential features of, the abrupt nature of backscatter fluctuations over space. Second, empty boundary cells of this surface model are filled with realizations of a Gaussian random process with the same global spectral characteristics of the backscatter data. Third, the surface model is windowed with overlap, and for each overlapping window the power spectrum is estimated using a discrete periodogram. Finally, a number of quantities are computed from the power spectra and mapped onto a new surface composed of discrete cells whose spatial position is governed by the size and spacing of overlapping windows.

Power spectra produce scale and amplitude metrics that collectively characterize the stochastic geometry of riverbed scattering. Treating scattering over small patches (up to a few meters) as a nonstationary random process, spectral analysis enjoys the advantages of being able to discriminate between data with identical distributions but different autocorrelations, and being unaffected by the specific spatial arrangement of the riverbed sediment patches (if frequency content remains the same, because the power spectra contain no phase information).

Backscatter power spectra obey a power law form; however, we argue that this does not necessarily indicate self-affine behavior (amplitude-to-length ratios are not independent of scale). We tentatively suggest that the use of combinations of stochastic geometries has a potential to delineate riverbed sediment patchiness given spatially explicit maps of these quantities at high resolution, in a data-driven approach comparing backscatter with bathymetric features and sediment observations. The use of spectral analysis requires no assumptions about the distributional form of the data nor a priori knowledge of the physical nature of riverbed scattering. It thus serves as a suitable means through which to classify bed sediment through a purely data-driven approach, which is the subject of Part 2.

Appendix A: Attenuation due to Sediment and Water

Attenuation due to suspended sediment is calculated according to *Urick* [1948], in dB^{-1} km:

$$\epsilon_s = \sum_a \phi_a \left(\frac{1}{6} k^4 a^3 + k(\sigma - 1)^2 \frac{s_a}{s_a^2 + (\sigma_a + \tau_a)^2} \right) \tag{A1}$$

$$\tau_a = \frac{1}{2} + \left(\frac{9}{4}\right)\left(\frac{\delta_\nu}{a}\right) \tag{A2}$$

$$s_a = \left(\frac{9}{4}\right)\left(\frac{\delta_\nu}{a}\right)\left(1 + \frac{\delta_\nu}{a}\right) \tag{A3}$$

where $\delta_\nu = 2\nu/\omega$; ν is the water viscosity ($\mathrm{m}^2\ \mathrm{s}^{-1}$); $\omega = 2\pi f$ is the radian frequency; f is the acoustic frequency (Hz); acoustic wave number $k = 2\pi/\lambda$; acoustic wavelength $\lambda = c/f$ (m); c is the speed of sound in

water (m s^{-1}); ϕ_a is the volumetric concentration of particle with radius a (m); $\sigma_a = \rho_s(a)/\rho$; and $\rho_s(a)$ and ρ are the densities (kg^{-1} m^3) of sediment of radius a and water, respectively.

Attenuation due to water is calculated, in dB^{-1} km, using [*Fisher and Simmons*, 1977]:

$$\epsilon = \frac{a_1 p_1 f_1 f^2}{f^2 + f_1^2} + \frac{a_2 p_2 f_2 f^2}{f^2 + f_2^2} + a_3 p_3 f^2 \tag{A4}$$

where:

$$a_1 = \frac{8.86}{c} 10^{(0.78pH-5)} \tag{A5}$$

$$a_2 = 21.44 \frac{S}{c}(1 + 0.025T) \tag{A6}$$

$$a_3 = (4.937 \times 10^{-4}) - (2.59 \times 10^{-5})T + (9.11 \times 10^{-7})T^2 - (1.5 \times 10^{-8})T^3 \tag{A7}$$

$$f_1 = 2.8\sqrt{S/35} \times 10^{(4-1245/T+273)} \tag{A8}$$

$$f_2 = \frac{8.17 \times 10^{(8-1990/T+273)}}{1 + 0.0018(S - 35)} \tag{A9}$$

$$p_2 = 1 - (1.37 \times 10^{-4})d + (6.2 \times 10^{-9})d^2 \tag{A10}$$

$$p_3 = 1 - (3.83 \times 10^{-5})d + (4.9 \times 10^{-10})d^2 \tag{A11}$$

where $p_1 = 1$; S is salinity (ppt); and T is temperature (°C).

Notation

a	Particle radius (m).
a_1, a_2, a_3	Attenuation coefficients.
A_f	Acoustic footprint.
b	Frequency bins.
B	Backscatter coefficient (dB).
c	Speed of sound in water (m s^{-1}).
d	Water depth below transducer (m).
e	Base of the natural logarithm.
EL	Echo level (dB).
f	Acoustic frequency (Hz).
f_1, f_2, f_3	Attenuation coefficients.
$\mathbf{F}$	$= \sqrt{F_X^2 + F_Y^2}$; Radial frequency vector (Hz).
$\mathbf{F}_b$	Bin averages of F (Hz).
g	Stochastic geometry.
h_0	Dimensional constant.
H	2-D Hann taper.
i	Imaginary unit.
k	$= 2\pi/\lambda$; Acoustic wave number.
k_X	Wave number in X direction.
k_Y	Wave number in Y direction.
$\mathbf{K}$	$= (k_X, k_Y)$; A two-dimensional wave vector.
l	Outer scale of the power law form of spectrum (m).
l_0	Integral length scale (m).
L	Lag index.
m	$= X/\Delta_X$; Indices of X.
n	$= Y/\Delta_Y$; Indices of Y.
N_s	Number of scatterers in insonified area.
N_X	Number of observations in X direction.

N_Y	Number of observations in Y direction.
p	Probability.
p_1, p_2, p_3	Pressure coefficients.
P_2	2-D power spectrum of $B(\mathbf{X})$.
P_1	1-D power spectrum of $B(\mathbf{X})$.
R	Angular range (m).
S	Salinity (ppt).
s_a	Sediment attenuation coefficient of sediment of radius a.
SL	Source level (dB).
t	Matrix transpose.
T	Temperature (°C).
TL	Transmission loss (dB).
T	Pulse duration (s).
W_2	2-D discrete Fourier transform of $B(\mathbf{X})$.
$\mathbf{x}$	Along-track beam vector.
X	Cartesian coordinate (m).
$\mathbf{X}$	Coordinate vector.
$\mathbf{y}$	Across-track beam vector.
Y	Cartesian coordinate (m).
α	Confidence interval.
β_x	Bed slope in the along-track direction (°).
β_y	Bed slope in the across-track direction (°).
χ_2	Chi-square probability distribution.
δ_v	$= 2\nu/\omega$.
$\Delta\psi$	Regular spacing of ψ (°).
Δ_X	Spacing of observations in X direction (m).
Δ_Y	Spacing of observations in Y direction (m).
ϵ	Sound attenuation due to water (dB km^{-1}).
ϵ_s	Sound attenuation due to sediment (dB km^{-1}).
γ_1	Spectral strength parameter (nondimensional).
κ	Tension factor (nondimensional).
λ	$= c/f$; Acoustic wavelength (m).
ν	Water viscosity (m^2 s^{-1}).
ω	$= 2\pi f$; Radian frequency (rads).
ω_1	Spectral strength parameter (dB^2).
Ω_x	Along-track beam aperture.
Ω_y	Across-track beam aperture.
ϕ_a	Volumetric concentration of particle with radius a (m).
ψ	Vector of angles over which spectral integration occurs.
ρ	Density of water (kg^{-1} m^3).
$\rho_s(a)$	Density of sediment of radius a (kg^{-1} m^3).
σ	Root-mean-square variance of $B(\mathbf{X})$ (dB).
σ_a	$= \rho_s(a)/\rho$.
τ_a	Sediment attenuation coefficient of sediment of radius a.
θ	Beam angle (°).
ξ_2	2-D autocorrelation function of $B(\mathbf{X})$.
∇	Laplacian operator.

Acknowledgments

Data and computer code to reproduce the results from this manuscript are available from the authors. The data analyzed and discussed in this manuscript were collected by the dedicated efforts of many field technicians, river guides, and volunteers. Special thanks to David Rubin, Robert Tusso, Peter Wilcock, and Joseph Hazel for data collection and discussions. This work was funded by the Glen Canyon Dam Adaptive Management Program administered by the U.S. Bureau of Reclamation. Any use of trade, product, or firm names is for descriptive purposes only and does not imply endorsement by the U.S. government. Thanks to the Editor, Associate Editor, Chris Sherwood, and two anonymous reviewers for their constructive comments which improved the quality of the paper.

References

Amiri-Simkooei, A., M. Snellen, and D. G. Simons (2009), Riverbed sediment classification using multi-beam echo-sounder backscatter data, *J. Acoust. Soc. Am.*, *126*, 1724–1738, doi:10.1121/1.3205397.

Anderson, J. T., D. V. Holliday, R. Kloser, D. G. Reid, and Y. Simard (2008), Acoustic seabed classification: Current practice and future directions, *ICES J. Mar. Sci.*, *65*, 1004–1011, doi:10.1093/icesjms/fsn061.

Brown, C. J., and P. Blondel (2009), Developments in the application of multibeam sonar backscatter for seafloor habitat mapping, *Appl. Acoust.*, *70*, 1242–1247, doi:10.1016/j.apacoust.2008.08.004.

Brown, C. J., S. J. Smith, P. Lawton, and J. T. Anderson (2011), Benthic habitat mapping: A review of progress towards improved understanding of the spatial ecology of the seafloor using acoustic techniques, *Estuarine Coastal Shelf Sci.*, *92*, 502–520, doi:10.1016/j.ecss.2011.02.007.

Buscombe, D., P. E. Grams, and M. A. Kaplinski (2014), Characterizing riverbed sediments using high-frequency acoustics 2: Scattering signatures of Colorado River bed sediments in Marble and Grand Canyons, *J. Geophys. Res. Earth Surf.*, doi:10.1002/2014JF003191.

Caress, D. W., and D. N. Chayes (1996), Improved processing of Hydrosweep DS multibeam data on the R/V Maurice Ewing, *Mar. Geophys. Res.*, *18*, 631–650.

Caress, D. W., and D. N. Chayes (2014), *MB-System Version 5, 2000–2014*, paper presented at Lamont-Doherty Earth Observatory, Columbia Univ., New York, Open source software distributed. [Available at http://www.ldeo.columbia.edu/MB-System, Accessed December 2012.]

Dietrich, W. E., and J. D. Smith (1984), Bed load transport in a river meander, *Water Resour. Res.*, *20*, 1355–1380, doi:10.1029/WR020i010p01355.

Dziak, R. P., H. Matsumoto, and C. G. Fox (1993), Estimation of seafloor roughness spectral parameters from multi-beam sonar acoustic backscatter data: Axial seamount, Juan De Fuca ridge, *Geophys. Res. Lett.*, *20*, 1863–1866, doi:10.1029/93GL01057.

Eleftherakis, D., A. Amiri-Simkooei, M. Snellen, and D. G. Simons (2012), Improving riverbed sediment classification using backscatter and depth residual features of multi-beam echo-sounder systems, *J. Acoust. Soc. Am.*, *131*, 3710–3725, doi:10.1121/1.3699206.

Fara, H. D., and A. E. Scheidegger (1961), Statistical geometry of porous media, *J. Geophys. Res.*, *66*, 3279–3284, doi:10.1029/JZ066i010p03279.

Fisher, F. H., and V. P. Simmons (1977), Sound absorption in seawater, *J. Acoust. Soc. Am.*, *62*, 558–564, doi:10.1121/1.381574.

Fonseca, L., C. Brown, B. Calder, L. Mayer, and Y. Rzhanov (2009), Angular range analysis of acoustic themes from Stanton Banks Ireland: A link between visual interpretation and multibeam echosounder angular signatures, *Appl. Acoust.*, *70*, 1298–1304, doi:10.1016/j.apacoust.2008.09.008.

Gallaudet, T. C., and C. P. de Moustier (2003), High-frequency volume and boundary acoustic backscatter fluctuations in shallow water, *J. Acoust. Soc. Am.*, *114*, 707–725, doi:10.1121/1.1588656.

Gilman, D. L., F. J. Fuglister, and J. M. Mitchell Jr. (1963), On the power spectrum of 'red noise', *J. Atmos. Sci.*, *20*, 182–184, doi:10.1175/1520-0469(1963)020<0182:OTPSON>2.0.CO;2.

Goff, J. A., and T. H. Jordan (1988), Stochastic modeling of seafloor morphology: Inversion of Sea Beam data for second-order statistics, *J. Geophys. Res.*, *B11*, 13,589–13,608, doi:10.1029/JB093iB11p13589.

Grams, P. E., D. J. Topping, J. C. Schmidt, J. E. Hazel, and M. Kaplinski (2013), Linking morphodynamic response with sediment mass balance on the Colorado River in Marble Canyon: Issues of scale, geomorphic setting, and sampling design, *J. Geophys. Res. Earth Surf.*, *118*, 361–381, doi:10.1002/jgrf.20050.

Guerrero, M., and A. Lamberti (2011), Flow field and morphology mapping using ADCP and multibeam techniques: Survey in the Po River, *J. Hydraul. Eng.*, *137*, 1576–1587, doi:10.1061/(ASCE)HY.1943-7900.0000464.

Hamilton, L. J., and I. Parnum (2011), Acoustic seabed segmentation from direct statistical clustering of entire multibeam sonar backscatter curves, *Cont. Shelf Res.*, *31*, 138–148, doi:10.1016/j.csr.2010.12.002.

Hellequin, L., J. M. Boucher, and X. Lurton (2003), Processing of high-frequency multibeam echo sounder data for seafloor characterization, *IEEE J. Oceanic Eng.*, *28*, 78–89, doi:10.1109/JOE.2002.808205.

Hough, S. E. (1989), On the use of spectral methods for the determination of fractal dimension, *Geophys. Res. Lett.*, *16*, 673–676, doi:10.1029/GL016i007p00673.

Jackeman, E. (1988), Non-Gaussian models for the statistics of scattered waves, *Adv. Phys.*, *37*, 471–529, doi:10.1080/00018738800101419.

Jackson, D. R. (1994), APL-UW high-frequency ocean environmental acoustic model handbook APL-UW TR 9407, *Appl. Phys. Lab. Tech. Rep.*, University of Washington, Washington, D. C.

Jackson, D. R., and M. D. Richardson (2007), *High-Frequency Seafloor Acoustics*, Springer, New York.

Jackson, D. R., K. B. Briggs, K. L. Williams, and M. D. Richardson (1996), Tests of models for high-frequency seafloor backscatter, *IEEE J. Oceanic Eng.*, *21*, 458–470, doi:10.1109/48.544057.

Jenkins, G. M., and D. G. Watts (1968), *Spectral Analysis and its Applications*, Holden-Day, San Francisco, Calif.

Kaplinski, M., J. E. Hazel, R. Parnell, M. Breedlove, K. Kohl, and M. Gonzales (2009), Monitoring fine-sediment volume in the Colorado River Ecosystem, Arizona: Bathymetric survey techniques, *U.S. Geol. Surv. Open File Rep. 2009–1207*, Flagstaff, Ariz.

Kaplinski, M., J. E. Hazel, P. E. Grams, and P. A. Davis (2014), Monitoring fine-sediment volume in the Colorado River ecosystem, Arizona: Construction and analysis of digital elevation models, *U.S. Geol. Surv. Open File Rep. 2014-1052*, Reston, Va.

Kloser, R. J., J. D. Penrose, and A. J. Butler (2010), Multi-beam backscatter measurements used to infer seabed habitats, *Cont. Shelf Res.*, *30*, 1772–1782, doi:10.1016/j.csr.2010.08.004.

Lamarche, G., X. Lurton, A.-L. Verdier, and J.-M. Augustin (2011), Quantitative characterisation of seafloor substrate and bedforms using advanced processing of multibeam backscatter—Application to Cook Strait, New Zealand, *Cont. Shelf Res.*, *31*, 93–109, doi:10.1016/j.csr.2010.06.001.

Le Gonidec, Y., G. Lamarche, and I. C. Wright (2003), Inhomogeneous substrate analysis using EM300 backscatter imagery, *Mar. Geophys. Res.*, *24*, 311–327, doi:10.1007/s11001-004-1945-9.

Lyons, A. P., and D. A. Abraham (1999), Statistical characterisation of high-frequency shallow-water seafloor backscatter, *J. Acoust. Soc. Am.*, *106*, 1307–1315, doi:10.1121/1.428034.

Matsumoto, H., R. P. Dziak, and C. G. Fox (1993), Estimation of seafloor microtopographic roughness through modeling of acoustic backscatter data recorded by multibeam sonar systems, *J. Acoust. Soc. Am.*, *94*, 2776–2787, doi:10.1121/1.407361.

Nelson, P. A., J. G. Venditti, W. E. Dietrich, J. W. Kirchner, H. Ikeda, F. Iseya, and L. S. Sklar (2009), Response of bed surface patchiness to reductions in sediment supply, *J. Geophys. Res.*, *114*, F02005, doi:10.1029/2008JF001144.

Nelson, P. A., D. Bellugi, and W. E. Dietrich (2014), Delineation of river bed-surface patches by clustering high-resolution spatial grain size data, *Geomorphology*, *205*, 102–119, doi:10.1016/j.geomorph.2012.06.008.

Nikora, V. I., D. Goring, and B. J. F. Biggs (1998), On gravel-bed roughness characterisation, *Water Resour. Res.*, *34*, 517–527, doi:10.1029/97WR02886.

Oppermann, N., M. Selig, M. R. Bell, and T. A. Enßlin (2013), Reconstruction of Gaussian and log-normal fields with spectral smoothness, *Phys. Rev. E*, *112*(032136), doi:10.1103/PhysRevE.87.032136.

Paola, C., and R. Seal (1995), Grain size patchiness as a cause of selective deposition and downstream fining, *Water Resour. Res.*, *31*, 1395–1408, doi:10.1029/94WR02975.

Parsons, D. R., J. L. Best, O. Orfeo, R. J. Hardy, R. Kostaschuk, and S. N. Lane (2005), Morphology and flow fields of three-dimensional dunes, Rio Parana, Argentina: Results from simultaneous multibeam echo sounding and acoustic Doppler current profiling, *J. Geophys. Res.*, *110*, F04S03, doi:10.1029/2004JF000231.

Perron, J. T., J. W. Kirchner, and W. E. Dietrich (2008), Spectral signatures of characteristic spatial scales and nonfractal structure in landscapes, *J. Geophys. Res.*, *113*, F04003, doi:10.1029/2007JF000866.

Priestley, M. B. (1981), *Spectral Analysis and Time Series*, Academic Press, New York.

Sayles, R. S., and T. R. Thomas (1978), Surface topography as a nonstationary random process, *Nature*, *271*, 431–434, doi:10.1038/271431a0.

Selig, M., M. R. Bell, H. Junklewitz, N. Oppermann, M. Reinecke, M. Greiner, and C. Pachajoa (2013), NIFTY—Numerical information field theory—A versatile Python library for signal inference, *Astron. Astrophys.*, *554*, A26, doi:10.1051/0004-6361/201321236.

Shields, F. D. (2010), Aquatic habitat bottom classification using ADCP, *J. Hydraul. Eng.*, *136*, 336–342, doi:10.1061/(ASCE)HY.1943-7900.0000181.

Simons, D. G., and M. Snellen (2009), A Bayesian approach to seafloor classification using multi-beam echo-sounder backscatter data, *Appl. Acoust.*, *70*, 1258–1268, doi:10.1016/j.apacoust.2008.07.013.

Smith, W. H. F., and P. Wessel (1990), Gridding with continuous curvature splines in tension, *Geophysics*, *55*, 293–305, doi:10.1190/1.1442837.

Snellen, M., D. Eleftherakis, A. Amiri-Simkooei, R. L. Koomans, and D. G. Simons (2013), An inter-comparison of sediment classification methods based on multi-beam echo-sounder backscatter and sediment natural radioactivity data, *J. Acoust. Soc. Am.*, *134*, 959–970, doi:10.1121/1.4812858.

Taylor, G. I. (1938), The spectrum of turbulence, *Proc. R. Soc. London Ser. A*, *164*, 476–490, doi:10.1098/rspa.1938.0032.

Torrence, C., and G. P. Compo (1998), A practical guide to wavelet analysis, *Bull. Am. Meteorol. Soc.*, *79*, 61–78.

Turcotte, D. L. (1997), *Fractals and Chaos in Geology and Geophysics*, Cambridge Univ. Press, New York.

Urick, R. J. (1948), The absorption of sound in suspension of irregular particles, *J. Acoust. Soc. Am.*, *20*, 283–289, doi:10.1121/1.1906373.

Urick, R. J. (1983), *Principles of Underwater Sound*, Peninsula Publ., Los Altos, Calif.

U.S. Army Corps of Engineers (2004), *Engineering and Design—Hydrographic Surveying*, 560 pp., U.S. Army Corps of Engineers Manual EM 1110-2-1003, Washington, D. C.

Van Rein, H. B., C. J. Brown, R. Quinn, and J. Breen (2009), A review of sublittoral monitoring methods in temperate waters: A focus on scale, *Underwater Technol.*, *28*, 99–113, doi:10.3723/ut.28.099.

Vericat, D., R. J. Batalla, and C. N. Gibbins (2008), Sediment entrainment and depletion from patches, *Water Resour. Res.*, *44*, W11415, doi:10.1029/2008WR007028.

Voss, R. (1988), Fractals in nature: From characterization to simulation, in *The Science of Fractal Images*, edited by H. O. Peitgen and D. Saupe, pp. 21–70, Springer, New York.

Wright, S. A., and M. Kaplinski (2011), Flow structures and sandbar dynamics in a canyon river during a controlled flood, Colorado River, Arizona, *J. Geophys. Res.*, *116*, F01019, doi:10.1029/2009JF001442.